Results in Surfaces and Interfaces 10 (2023) 100098

Contents lists available at ScienceDirect

Results in Surfaces and Interfaces

journal homepage: www.elsevier.com/locate/rsurfi

Development and characterizations of Ag nanoparticles decorated TiO_2-ZrO_2 coatings as electrode material for supercapacitors

Sanu Mathew Simon [a,b], Prakashan V.P. [c], Sajna M.S. [d], Anoop Chandran [e], Gejo George [f], Eric K. Barmiah [g], Gin Jose [g], Biju P.R. [a], Cyriac Joseph [a], Unnikrishnan N.V. [a,*]

[a] School of Pure & Applied Physics, Mahatma Gandhi University, Kottayam 686 560, India
[b] Institute for Integrated Programmes and Research in Basic Sciences, Mahatma Gandhi University, Kottayam 686 560, India
[c] Department of Physics, Sree Kerala Varma College, Thrissur 680 011, India
[d] Centre for Advanced Materials, Qatar University, P.O. Box 2713, Qatar
[e] Department of Physics, St. Cyril's College, Adoor, India
[f] Department of Chemistry, St. Berchman's College, Changanassery 686 101, India
[g] School of Chemical and Process Engineering, University of Leeds, Leeds LS2 9JT, United Kingdom

ARTICLE INFO

Keywords:
Energy storage
Cyclic voltammograms
TiO_2-ZrO_2 films
Double-layer electrical capacitance
Self-cleaning

ABSTRACT

Supercapacitors are considered as newly developed auxiliary and clean supplies of power and energy for the next generation energy storage devices with significant impact in many fields. In the present investigation, Ag nanoparticles decorated over TiO_2-ZrO_2 films are used as the material for energy storage applications. The cyclic voltammograms of the proposed material show better specific capacitance values and robust cyclic stability. The results of the electrochemical measurements further show a strong double-layer electrical capacitance of ternary mixed oxides. The synergetic interaction among the components in the hierarchical nanostructured porous Ag@TiO_2-ZrO_2 film guaranteed the good capacitive performance. The comparison between the TiO_2-ZrO_2 films and Ag decorated TiO_2-ZrO_2 films bring out the strong interconnection between the constitution and composition of both systems and their properties. These results underline the exceptional electrical double layer capacitive behavior that is seen in porous ternary composite films with better surface area. Furthermore, such a simple and low-cost layer by layer assembly method with self-cleaning property can be used for the large-scale fabrication of diverse functional architectures for energy storage and conversions.

1. Introduction

The rapid growth in universal economy and industry can cause the energy crisis in the near future which inspires intense investigations on the effective, reliable, low-cost, and environmental friendly energy storage resources (Giri et al., 2014; Liu et al., 2017; Padmanathan and Selladurai, 2014). As a result, a lot of works have been dedicated to develop low-cost electrode materials with high power density, high energy density, long service life, etc (Li et al., 2019; Biswal et al., 2013; Liu et al., 2013; Huang et al., 2014; Wu et al., 2019a; Pang et al., 2000). To improve the performance and practical applicability, many active materials have been investigated to fabricate supercapacitor electrodes, which can be normally divided into two categories based on the mechanism of the capacitor, electrical double layer capacitors (EDLCs) and Faradaic redox reaction pseudocapacitors (Barik et al., 2017; Selvakumar et al., 2017).

Because of the inherent demerits like poor electrical conductivity, material pulverization of metal oxides, more and more efforts have been devoted to improve the performance of metal oxide based electrodes by forming binary metal oxide composites. The main merits shown by mixed transition metal oxides are (i) they possess better electrical conductivity than pure metal oxides due to their relatively less activation energy for electron transfer and (ii) they also own richer redox active sites owing to mixing of two metal species (Reddy et al., 2013; Mai et al., 2014; Li et al., 2016; Zhang et al., 2015). The synergistic effect of pure oxides enhances the capacitive behavior of binary transition metal oxides with a widened potential window, better conductivity, more active sites and enhanced stability. These specialties are significant for electrochemical materials since its versatile structure can provide contact between electrode and electrolyte at the interface. Moreover, the porous structure permits the liquid electrolyte to diffuse effortlessly into the electrode materials (Weng et al., 2013).

Among various transition metal oxides, TiO_2 nanostructures have fascinated wide attention among researchers because of their peculiar structure, which can offer shorter pathways for electron transfer, decrease in the resistance provided during electron-transfer, and then

* Corresponding author.
E-mail address: nvu100@yahoo.com (Unnikrishnan N.V.).

https://doi.org/10.1016/j.rsurfi.2023.100098
Received 24 September 2022; Received in revised form 23 December 2022; Accepted 10 January 2023

Table 1
Surface atomic concentrations (percentage) from XPS data.

Sample code	Carbon at %	Oxygen at %	Titanium at %	Zirconium at %	Ag at %
Ag@TZPF	52.47	39.28	8.13	0.11	~ 0.01
TZPF	46.80	46.12	6.04	1.04	–

enhance the pace of electron-transfer rate as well as the electrical conductivity (Weng et al., 2013; Parveen et al., 2017). Most works reported on TiO_2 are the composite formation with carbonaceous materials like graphene, carbon nanotube, etc (Toledo et al., 2019; Brezesinski et al., 2009; Wu et al., 2019b). For example, Sun et al. prepared TiO_2 nanoparticle coated graphene sheets as electrode materials to achieve a specific capacitance of 75 F/g (Sun et al., 2012). Liu et al. worked on graphene oxide (GO)/TiO_2 nanorod composite to fabricate supercapacitor electrode with a specific capacitance of 100 F/g (Liu et al., 2015). Ramadoss and co-workers reported the development of graphene-TiO_2 hybrid electrode with a specific capacitance value of 165 F/g (Ramadoss and Kim, 2013). The main disadvantages of fabricating hybrids of TiO_2 and other carbon-based materials are that they inevitably require complicated methods that incur high cost, lengthy processing times, and moreover the need for bulky equipment.

However, the poor capacitive nature of TiO_2 limits its practical use. The wide bandgap of TiO_2 would be the reason for the meager efficiency and low conductivity seen in the reported works (Zhang et al., 2019; Azizi et al., 2019). Hence, It would be very exciting to intercalate TiO_2 with another metal oxide to collectively improve the electrical conductivity as well as capacitive properties of the TiO_2 based electrode for supercapacitor (Weng et al., 2013; Wu et al., 2019b; Park et al., 2020; Guo et al., 2019). The composite formation of ZrO_2 with carbonaceous materials aroused great interest in fabricating electrode material for high-power energy storage material (Mudila et al., 2016; Elmouwahidi et al., 2018). Eventhough these outcomes are exciting, capacitive energy storage in bulk films can be delayed by slow molecular transport of solvents and ions via the film structure. To solve this problem, films with porosity are developed via template assisted synthesis using structure directing agents Pluronic F127 and poly (methyl methacrylate).

On the other hand, the deposition of Ag nanoparticles over porous TiO_2-ZrO_2 composites has increased the capacitance of composite electrodes owing to their high electrical conductivity, Faradaic behavior, and high surface area.[28] Herein, the synthesis of Ag@TiO_2-ZrO_2 ternary composite over ITO substrates via sol–gel assisted dip coating method as an electrode for the fabrication of supercapacitor with enhanced capacitive energy storage is reported. We have found our attention to characterize the prepared materials in respective of capacitive behavior and self cleaning nature which are essential for supercapacitor applications. The as-prepared Ag@TiO_2-ZrO_2 composite coatings possessed enhanced specific capacitance and improved rate capacity which can be attributed to the synergistic effect of the pseudo-capacitance of TiO_2-ZrO_2 and Ag nanoparticles (Zhang et al., 2019).

2. Experimental details

Titanium (IV) isopropoxide 97%, Zirconium (IV) propoxide solution, Pluronic F127, N, N-Dimethyl formamide anhydrous 99.8%, Acetylacetone 99% were procured from SIGMA ALDRICH. Poly (methyl methacrylate) $[CH_2C(CH_3)(CO_2CH_3)\text{-}]_n$ and Diethanolamine 99% brought from Alfa Aesar. Silver nitrate was procured from MERCK whereas Ethyl Alcohol AR 99.9% v/v was purchased from Hayman chemical company. Poly (vinyl pyrrolidone) K-25 $(C_6H_9NO)_n$ was purchased from Central Drug house (P)LTD, New Delhi.

Double templated TiO_2-ZrO_2 coatings were developed using sol–gel assisted dip coating technique over ITO substrates as reported in our earlier work (Simon et al., 2018; Hareesh et al., 2020). The prepared films were kept for heating at 150 °C for 24 h and the end product was coded as "TZPF". $AgNO_3$ solution (0.05 M) was prepared by following the procedure reported by Dutta et al. (2013) Layer by layer assembly of the coatings was introduced for the development of templated porous Ag decorated TiO_2-ZrO_2 coatings and the final product was coded as "Ag@TZPF".

The cross-sectional elemental mapping of the films was done by Oxford Instruments INCA 350 energy dispersive spectroscopic system/80 mm X-Max SDD detector and Gatan Orius SC600 A CCD camera. The chemical composition of the films was verified with X-ray photoelectron spectroscopy (XPS) analysis (Kratos analytical X-ray photoelectron spectrometer). The surface morphology and micro structure were characterized by field emission scanning electron microscope (FESEM, ZESIS-$\sum$ IGMA) and high-resolution transmission electron microscopy (TEM) (JEOL JEM 2100, operating at 200 kV), respectively. Atomic Force Microscope (Nanoscope IIIa, Optical Instrument, USA) working in taping mode with a silicon tip was used to investigate the surface relief of the films. Cyclic voltammograms (CV) and impedance studies were obtained through the three-electrode workstation Biologic SP-200. Here, measurements were carried out using 0.1 M H_2SO_4 electrolyte with Pt as the counter electrode and Ag/AgCl as the reference electrode. Different mediums of electrolyte solution was also checked and optimized acidic medium as most fit choice.

3. Results and discussion

3.1. Textural and chemical analysis of the TiO_2-$ZrO_2$and Ag@TiO_2-ZrO_2 composite thin films

Mesostructured Ag@TiO_2-ZrO_2 composites developed via layer by layer assembly attain great interest due to their desirable merits, such as high surface area, pore size and morphology. Fig. 1 provides the elemental mapping images associated with HAADF-STEM imaging which reveal insights into the composition of the coatings. The elemental mapping images show that both the Ti as well as Zr elements are enriched in the prepared bi-layered structure. In addition, the Ag elements are also observed to be homogeneously distributed over the coatings as a layer and the interfaces between the layers are well clear in the images. EDX spectrum also confirms the presence of all elements in the Ag nanoparticles decorated TiO_2-ZrO_2 coatings.

More comprehensive studies on the elemental composition of the synthesized samples were done using X-ray photoelectron spectroscopy. The XPS scans were performed for C 1s, Ag 3d, Zr 3d, Ti 2p, and O 1s (Fig. 2) to examine the composition of synthesized composite films and confirm that all the elements exist on the surface.

The peak position for Ti 2p exists at around 456.8 eV for TZPF as well as for Ag@TZPF films, whereas for the same films peak position for Zr 3d exists near to 181.95 eV. The peak position for Ti 2p and Zr 3d of Ag@TZPF films demonstrate no significant change compared to that of TZPF. The signals at 530.54 eV and 528.48 eV are attributed to O 1s of TZPF and Ag@TZPF films, respectively. Similarly, the peak positions at 285.49 eV and 283.47 eV shown in the spectra of TZPF and Ag@TZPF films respectively correspond to adventitious carbon. The small intense peak observed around 345.26 eV can be ascribed to the presence of Ag nanoparticles. The peak for all elements increased in intensity compared to pure TZPF films. It can therefore be assumed that both films consist of elements Ti, Zr, C and O whereas Ag is present in Ag@TZPF film, which is in strong correlation with the above EDX. The calculated values of surface concentrations for all the elements in the atomic percentage are given in Table 1. Detailed XPS analysis of the TZPF films were reported in our previous work (Simon et al., 2018; Zhang et al., 2022b).

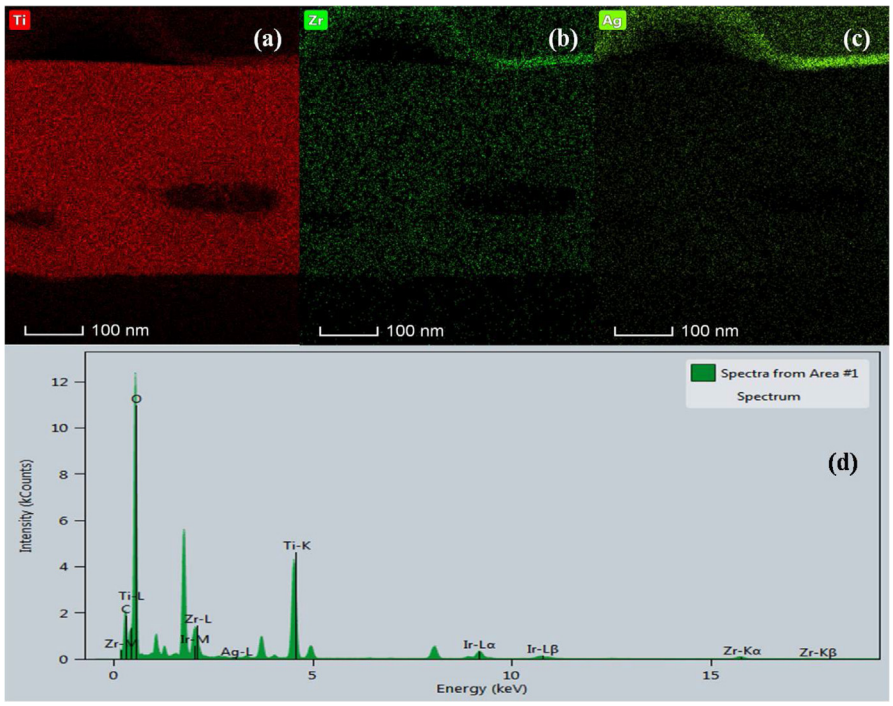

Fig. 1. EDS mapping images assisted with cross-sectional HAADF-STEM images of Ag@TZPPF films. (a) Ti (b) Zr (c) Ag and (d) the corresponding EDS spectrum.

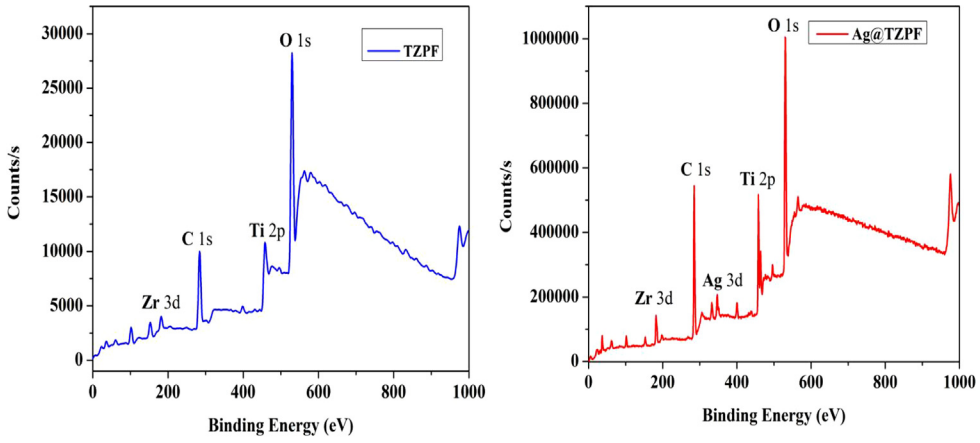

Fig. 2. XPS wide-scan survey spectra of (a) TZPF (b) Ag@TZPF thin films.

The prospect of morphology and structure of TZPF and Ag@TZPF films were examined by AFM analysis and shown in Fig. 3. The images reveal that the films are regular and continuous one. The parameters related to the surface roughness from the AFM analysis are summarized in Table 2. The decoration of Ag nanoparticles with homogeneous distribution over the surface is clearly evidenced in Fig. 3(a). After the incorporation of Ag nanoparticles over TZPF films, the surface roughness values changed from 126.16 to 43.94 nm. The increase in grain size is clearly visible in the images which are in good agreement with FESEM as well as TEM analyses discussed in the latter section. The parameters kurtosis and skewness represent the peakedness of the surface. Silver decoration over TZPF films will provide a peculiar architecture for the films which is clearly evident from the parameters tabulated in Table 2. The images deliver basic insight into the morphology and structural parameters of the two films which even invite further investigations.

The size, shape and distribution of Ag nanoparticles deposited over TZPF films in comparison with pure TZPF films were evaluated using FESEM analysis. Fig. 4(a)–(d) shows the FESEM images of pure TZPF films and Ag@TZPF films. The ordinary TZPF film appears smooth but porous in nature and thickness of the TZPF film is obtained from the cross-sectional image as 1.1 μm shown in Fig. 4(b). Roughened structure arises due to the porosity which offers more surface and nucleation location for the synthesis of Ag NPs. Meanwhile, it is observed that in Ag@TZPF films, the smooth surface possesses numerous Ag nanoparticles in different shapes and these particles are well covered and densely populated over the surface. Higher magnified image (Fig. 4(c)) reveals the hierarchical distribution of Ag nanoparticles with different shapes which predominantly consist of trigonal tabular form whereas, at the same time the presence of hexagonal shaped NPs is also noted.

Table 2
Surface roughness parameters from AFM analysis.

Sample code	Average roughness (nm)	Root mean square roughness (nm)	Kurtosis	Skewness
TZPF	126.16	168.06	−0.0241	5.06
Ag@TZPF	43.94	55.82	−0.7439	6.36

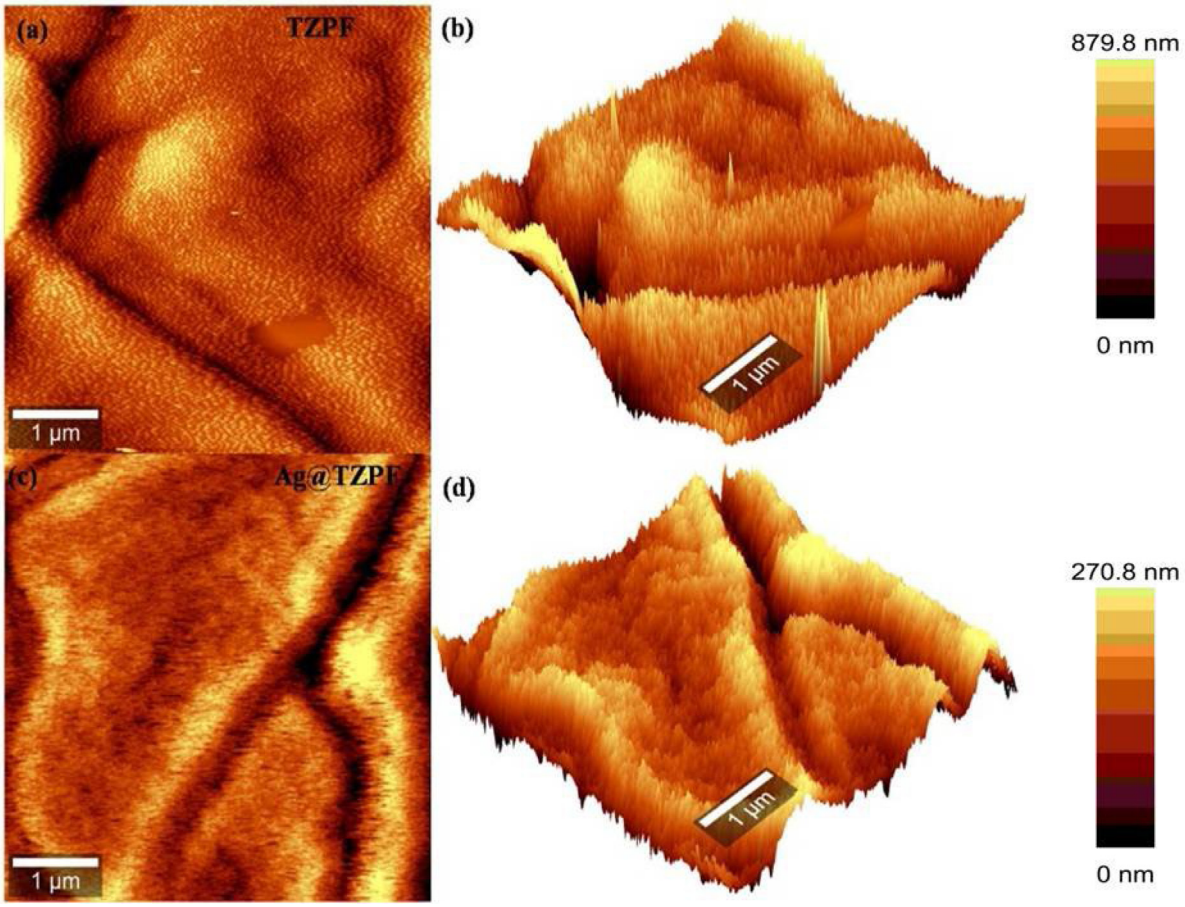

Fig. 3. 2D AFM images of (a) TZPF (c) Ag@TZPF films and 3D AFM images of (b) TZPF (d) Ag@TZPF films.

The fascinating morphology observed for the nanoparticles is mainly attributed to the synthesis procedure of chemical reduction method and the special capping agent used. The closely connected nanoparticles cover the matrix and can produce new pathways for conduction which enhance electrical conductivity. On the other hand, the nanoparticles show the tendency of aggregation which may reduce the conductivity. The aggregation could be hindered by covering Ag nanoparticles over TiO_2-ZrO_2 coatings.

In order to further study the morphology and crystalline nature of the Ag@TZPF films, TEM analysis was carried out and the corresponding micrographs are shown in Fig. 5. TEM images confirm the presence of Ag nanoparticles and also it is well clear that these nanoparticles are well embedded over TiO_2-ZrO_2 matrix. The nanoparticles with different shapes in the matrix are clearly visible in the images. From Fig. 5(a), it is clearly evident that there exist two types of populations of Ag nanoparticles in Ag@TZPF film: larger trigonal Ag NPs and smaller spherical NPs. As shown in the histogram of particle size distribution (Fig. 6(a) and (b)), the most number of spherical shaped nanoparticles exhibit diameter in the range 20–30 nm while the length of trigonal shaped NPs exists in the range 170–220 nm. Hence, a better interaction between Ag nanoparticles and TiO_2-ZrO_2 matrix is possible which may favor the transfer of electrons to enhance the electrical conductivity of the entire system. The specific capacitance shows large dependence on the size and morphology of nanoparticles since smaller particles possess larger surface area resulting in the higher specific capacitance value. In addition, TiO_2-ZrO_2 matrix prevents the agglomeration of Ag nanoparticles which will be beneficial for the enhancement of capacitive performance as evident from the TEM images. Furthermore, SAED pattern (Fig. 5(f)) reveals that Ag@TZPF composite films show a distinct set of lattice fringes. The inter-planar spacings of 0.143 nm and 0.234 nm correspond well with planes (2 2 0) and (1 1 1) of cubic Ag nanoparticles (ICDD No. 04–0783) whereas 0.273 nm and 0.351 nm correspond to tetragonal TiO_2 (ICDD No. 89–4203). The d-spacing of 0.119 nm, 0.175 nm, and 0.202 nm depicts the lattice planes (1 1 4), ($\bar{2}$ 2 1) and (1 1 2) of monoclinic ZrO_2 (ICDD No. 04–0783) (Zhang et al., 2022a).

3.2. *Electrochemical behavior of the synthesized TiO_2-ZrO_2 and Ag@TiO_2-ZrO_2 composite thin films*

The development of ternary metal composite as an electrode for supercapacitors is an alternative method apart from the wide usage of carbon materials and conducting polymers for the fabrication of the electrode (Azizi et al., 2019; Guo et al., 2019). The electrodes with weak electronic conductivity adversely affect the rapid interface reaction. Therefore, in the proposed ternary composite film, AgNPs exhibit high electronic conductivity while TiO_2-ZrO_2 offers structural as well as thermal stability. Hence, ternary composite film will show improved electro-chemical performance. Additionally, Pluronic F127 also plays a vital role by the creation of porosity which enhances the capacitive storage of the films (Brezesinski et al., 2009).

Electrochemical experiments were carried out to explore the properties of the film in the background of supercapacitor application. Cyclic voltammetry (CV), galvanostatic charging and discharging and EIS measurements were conducted to find the advantages of film as electrochemical electrode with a three electrode cell in an acidic medium (Anil et al., 2020). Herein, measurements were performed by considering Pt as the counter electrode and Ag/AgCl as the reference electrode in 0.1 M H_2SO_4 electrolyte (Parveen et al., 2017). With this approach, good accessibility between the H_2SO_4 electrolyte and the

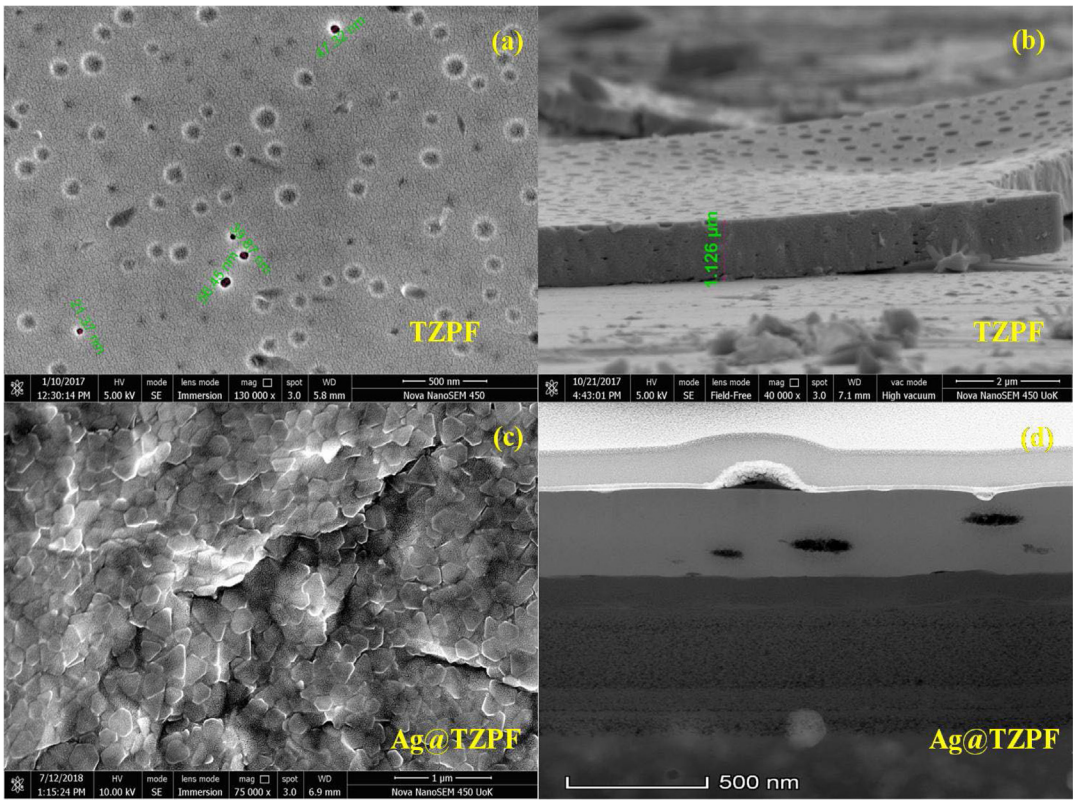

Fig. 4. FESEM and cross sectional image of TZPF films (a and b) Ag@TZPF films (c and d).

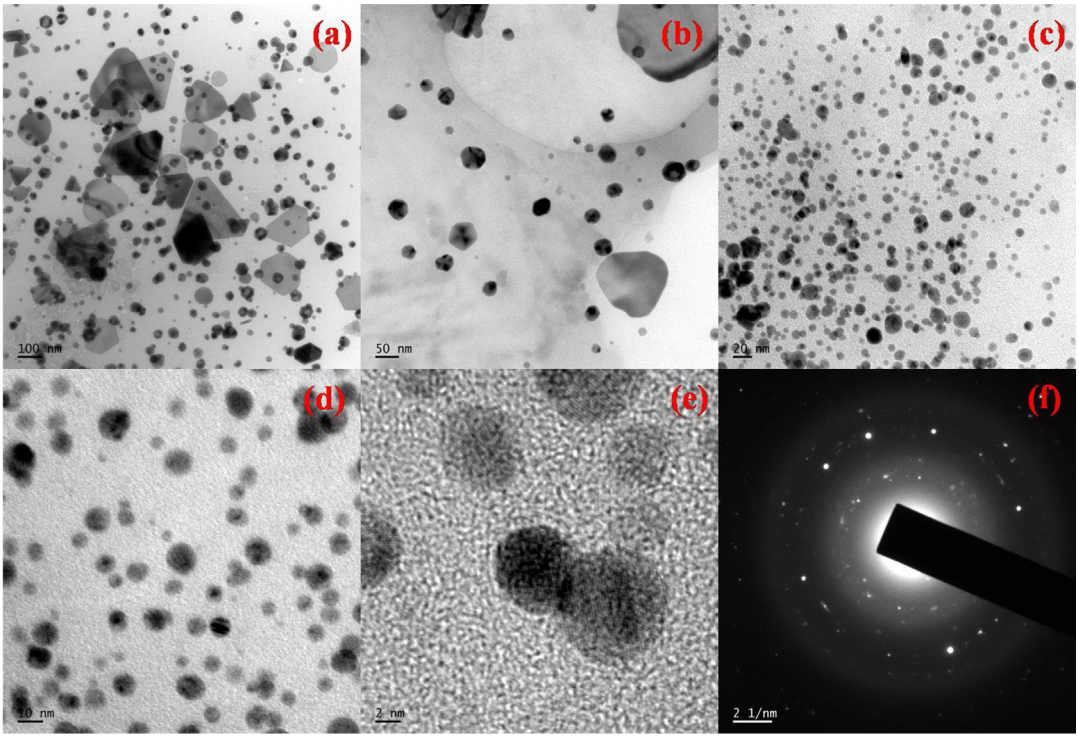

Fig. 5. (a)–(e) TEM micrographs (f) SAED pattern of Ag decorated TZPF films.

as-synthesized electrodes is expected to end in advanced capacitive performance. Fig. 7 represents typical cyclic voltammograms of ZPF, TPF, TZPF and Ag@TZPF films at room temperature in the potential range 0.12 V to 0.55 V. The CV plot for Ag@TZPF film shows nearly perfect rectangular shape with large area representing better capacitive properties compared to the shape of other films. Furthermore, the potential window for Ag@TZPF film shows symmetric shape and also the current density exhibits increasing trend. The large surface area, porosity and Ag nanoparticles acting as channels may be the reason for the enhancement of the capacitance in the case of Ag@TZPF films.

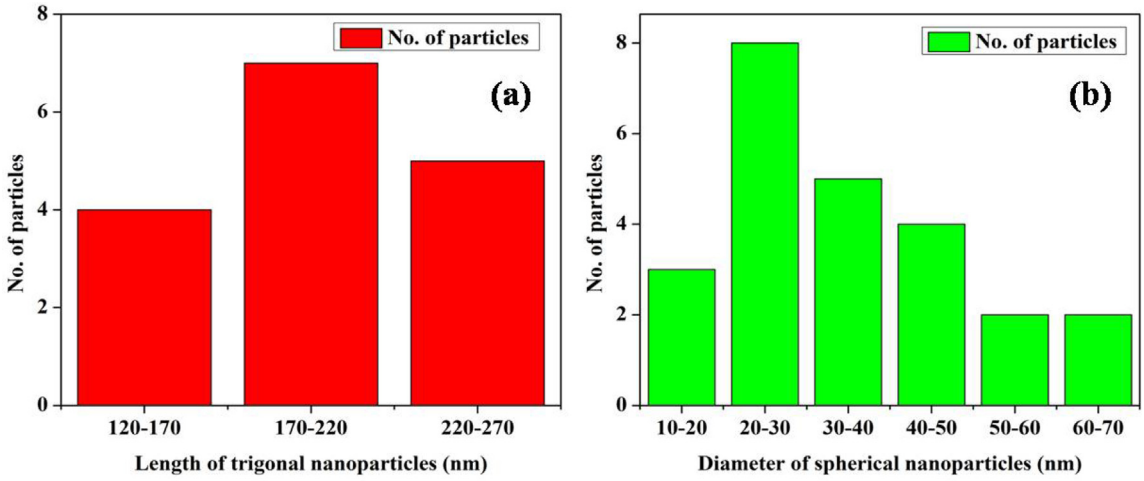

Fig. 6. Histogram of particle size distribution (a) trigonal nanoparticles (b) spherical nanoparticles.

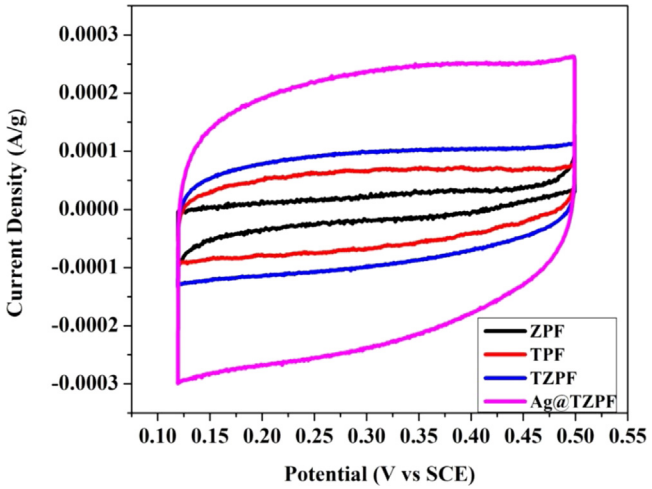

Fig. 7. Comparison of cyclic voltammetric response of ZPF, TPF, TZPF and Ag@TZPF films.

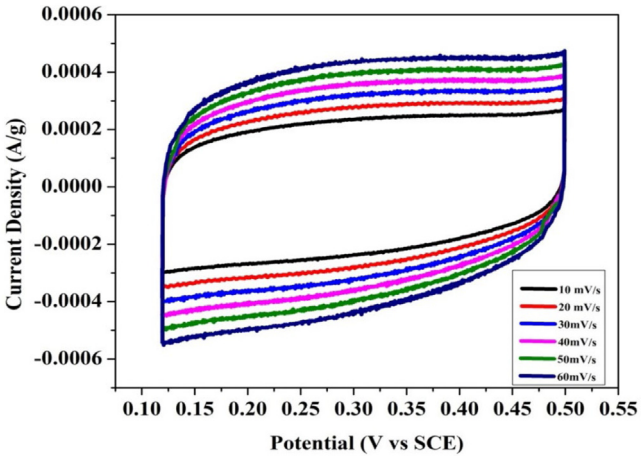

Fig. 8. Scan rate dependent CV curves for Ag@TZPF films.

The ions from the H_2SO_4 electrolyte could insert/desert into/from the Ag nanoparticles acting as channels between TiO_2-ZrO_2 matrix to store or release energy. Such a method of penetration of these ions into the porous matrix results in the heavy loading of these ions in the small pores. This strong confinement would provide a distorted solvated ionic shell that leads to superior interaction between the entire matrix which acts as an electrode and the trapped charged ions of the electrolyte directing to an increase in the value of the supercapacitance (Biswal et al., 2013; Raveesha et al., 2019). In a clear way, it can be said that the capacitance of Ag@TZPF in H_2SO_4 aqueous electrolyte mostly arises from the formation of an electrical double layer. It resulted from the reversible adsorption and desorption of the ions occurring within the spacers of Ag nanoparticles and TiO_2-ZrO_2 matrix. The porous semi-conductive TiO_2-ZrO_2 matrix in the ternary composite provides high energy storage capacity by holding Ag nanoparticles collapsing and aggregating. Also, the highly conductive Ag nanoparticles allow the electron transport and easy ion diffusion into the core of TiO_2-ZrO_2 matrix (Giri et al., 2014).

Fig. 8 depicts the scan rates dependent cyclic voltammetry curves of optimized Ag@TZPF sample in the range 0.1 V s^{-1}- 0.55 V s^{-1}. From the figure, it can be noted that the integral area under the CV responses slightly increases with the stepwise increase in scan rate, signifying better rate capability of the Ag@TZPF electrode. Besides that, anodic and cathodic peak current densities of the film are linearly proportional to the scanning rate, implying that the electrochemical activity of the electrode is due to the mechanism of the adsorption control process. At the very same time, as the scan rate increased the anodic as well as cathode peak potential shows a minor shift. This shift for peak potential may be arising from the slow electron transfer due to the electrode formed from the heterogeneous surface.[27] The electron exchange that occurred at the metal/semiconducting matrix and metal/solution interfaces also contributes to this shift (Giri et al., 2014).

CV plots have also been used to compute the values of specific capacitance (Cs in F/g) of the films. The capacitance (C) of an electrode may be calculated using the relation (Giri et al., 2014),

$$C_s = \frac{C}{m} = \frac{\int_{V_1}^{V_2} i\,(V)\,dV}{(V_2 - V_1)\,m}. \quad (1)$$

where the numerator part of the above equation shows the area of CV curve and V_1, V_2 are the switching potential in cyclic voltammetry and m represents the mass of the film. The specific capacitance of Ag@TZPF films was calculated as 237.13 F/g, whereas that of TZPF sample the value is 59.82 F/g. These results revealed that a better storage energy capacity for the film at low current is possible. The specific capacitance value of Ag@TZPF films is nearly four times higher than that of TZPF films. The specific capacitance value for pure TiO_2 as well as ZrO_2 films was also very low. The rise in the specific capacitance value for the Ag@TZPF film electrodes is due to the improvement in

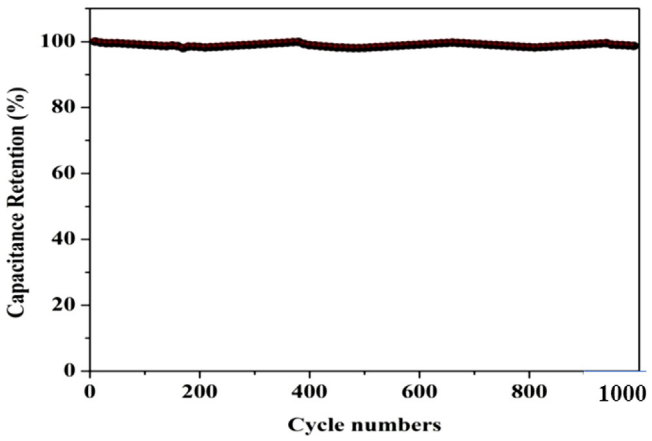

Fig. 9. Capacitance retention with number of cycles.

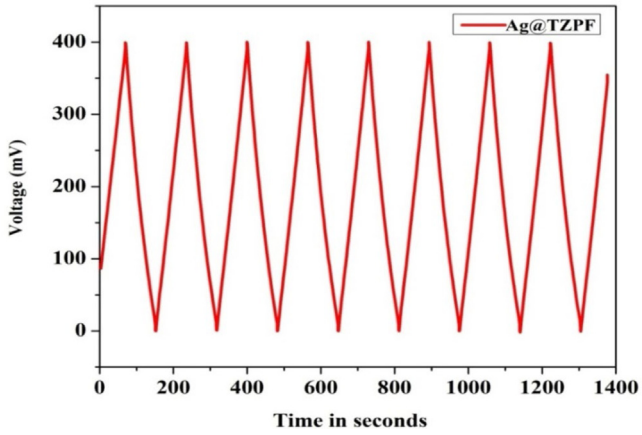

Fig. 10. Galvanostatic charge–discharge curves of Ag@TiO_2-ZrO_2 films.

the insertion of ions on the surface of the electrode material. Besides, the natural dispersion of AgNPs over TiO_2-ZrO_2 helps to improve the ionic conductivity of the composite. The significantly improved specific capacitance was attributed to the synergistic effects of the Ag nanoparticles and TiO_2-ZrO_2 matrix as well as the porosity produced by the particular method of synthesis adopted for the composite film.[17] In addition, the synthesis method and the porosity will amplify the specific surface area of the sample and facilitates ion diffusion from the solution to the surface of the electrode material. The present work is the first report on the development and performance studies of Ag decorated TiO_2-ZrO_2 films as an electrode for the supercapacitors. The proposed Ag decorated TiO_2-ZrO_2 films could show better retainability of its novel specific capacity even after 1000 cycles as shown in Fig. 9. During the repeated cycles, a slight drop in the cyclic stability of the proposed device can be due to a moderate loss of its electroactive sites (Sundriyal et al., 2019). The galvanostatic charge/discharge curves of Ag@TiO_2-ZrO_2 film at a current density of 0.2 mAg^{-1} is shown in Fig. 10. These charge/discharge plots are almost nearly linear across the wide range of potential with constant slopes, describing ideal electrocapacitive behavior. The introduction of Ag nanoparticles had afforded TiO_2-ZrO_2 matrix to attain such an improved electrochemical activity with good stability.

Electrochemical impedance spectroscopy (EIS) measurements for ZPF, TPF, TZPF and Ag@TZPF films were performed using three electrode system in 1 M H_2SO_4 within the frequency range from 1–100 MHz. Nyquist plots for the films are shown in Fig. 11 and the corresponding parameters obtained are tabulated in Table 3. The impedance

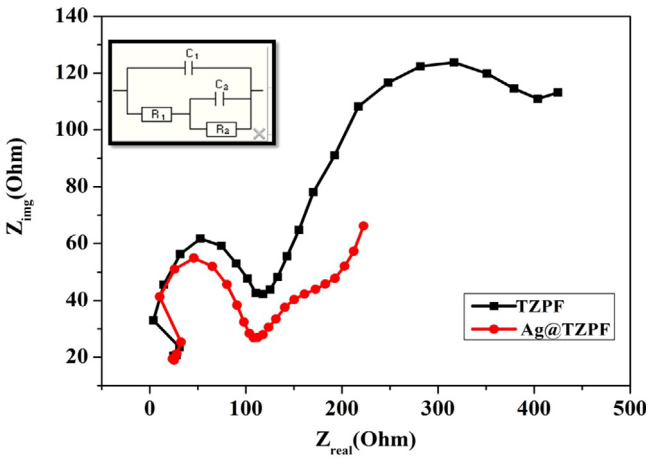

Fig. 11. Nyquist plot of TZPF and Ag@TZPF films. Inset equivalent circuit.

Table 3
EIS fitted parameters.

Sample code	R_s (Ω)	R_{ct} (Ω)	W (Siemens × $Seconds^{1/2}$)
TZPF	26.58	87.89	85.2
Ag@TZPF	26.92	82.08	97.9

of an electrode is generally represented by

$$Z(w) = Z_{real} + jZ_{img} \quad (2)$$

where Z_{real} and Z_{img} are the real and imaginary parts of the impedance. The actual Z_{real} component uncovers the ohmic properties, whereas the imaginary part (Z_{img}) corresponds to the capacitive properties (Kotteeswaran et al., 2017). The intersection of Nyquist plot at the x-axis generally gives the solution resistance of the electrochemical system (R_s). Meanwhile, the charge transfer resistance (R_{ct}) can be measured from the diameter of the semicircle. Warburg impedance (W), which is a testimony of the diffusion of electrolyte into the active materials, can be evaluated using the slope of the line. In the present case, it is seen that the solution resistance values of both electrodes are identical. Moreover, semi-circles with larger radii usually refer to higher charge transfer resistance of the electrode (Kumar et al., 2019). Consequently, the EIS result suggests that the charge transfer resistance R_{ct} of the Ag@TiO_2-ZrO_2 electrode is much lower than that of TiO_2-ZrO_2 which implies a lower charge transfer resistance for Ag@TZPF films compared to TZPF films and therefore has more capacitive properties. These values strongly demonstrate the higher conductivity of Ag@TiO_2-ZrO_2 films and sequentially represent the better accommodation and transportation of ions in the composite (Giri et al., 2014). Simpler ionic conduction/ transportation throughout the matrix is an important requisite for the development of ideal supercapacitors.

To analyze the different electrochemical parameters involved along with corresponding electrochemical phenomena that occur within the electrode, the Nyquist plots obtained can be fitted with an equivalent electrical circuit. The impedance of the system can be represented (Brug et al., 1984; Viswanathan et al., 1995) as

$$Z_{CPE} = \frac{1}{Y(j\omega)^n} \quad (3)$$

where ω depicts the angular frequency in rad s^{-1}, Y and n are adjustable parameters of constant phase element (Q_1). The $n = 1$ value shows the double layer capacitance, $n = 0$ matches to the resistance and $n = 0.5$ refers to Warburg diffusion. Thus, a model consisting of constant phase element should be used to fit the data into the corresponding circuit (inset of Fig. 11). From the accessible data, it is quite evident that Ag@TZPF film shows features of high double layer capacitance and low

Table 4
Comparison of the present work with previous reports.

System name	Synthesis method used for synthesis	Specific capacitance (F/g)	Reference
Nanoscale coating of TiO_2 on graphene	Atomic layer deposition	84 at 10 mV/s	Sun et al. (2012)
TiO_2 nanorods loaded on graphene oxide	Two phase self-assembly approach	100 at 5 mV/s	Liu et al. (2015)
Graphene-TiO_2	Microwave assisted approach	165 at 5 mV/s	Ramadoss and Kim (2013)
Polypyrrole wrapped graphene/TiO_2 hydrogels	Hydrothermal and polymerization	300 at 0.5 A/g	Zhang et al. (2019)
Reduced graphene oxide/ TiO_2 nanosheet	Hydrothermal reaction	204 at 1.5 A/g	Sundriyal et al. (2019)
TiO_2-Graphene hydrogel	One pot hydrothermal approach	34.8 at 5 mV/s	Viswanathan et al. (1995)
Ag incorporated rGO@TiO_2	High temperature and chemical reduction method	345 F/g	Zhang et al. (2013)
Two-dimensional nickel-cobalt layered double hydroxides	sodium dodecyl sulfate (SDS) intercalation modification	91% after 10,000 cycles at 5 A g^{-1}	Zhang et al. (2023)
Ag@TiO_2-ZrO_2 films	Sol–gel assisted dip coating method	237 at 10 mV/s	This work

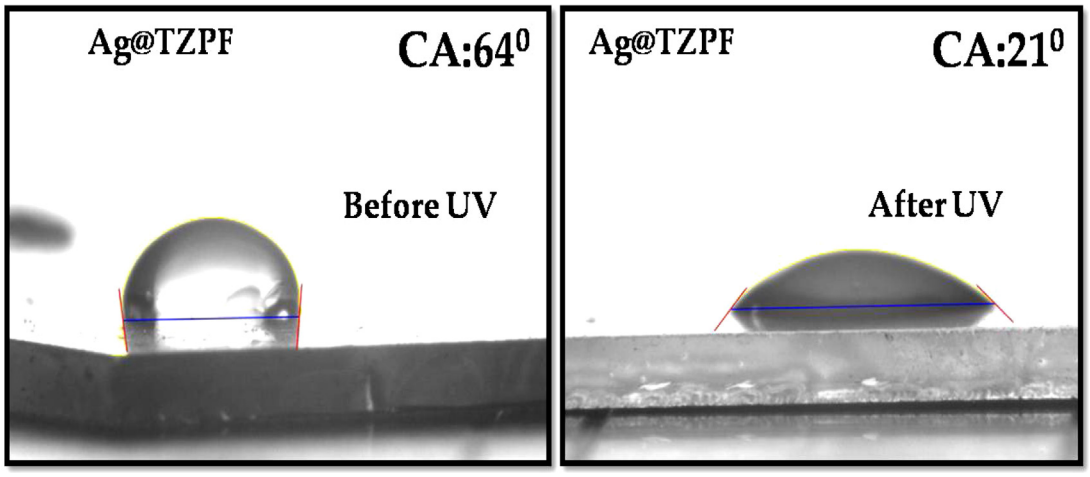

Fig. 12. Contact angle measurements of Ag@TZPF films.

charge transfer resistance. Moreover, from the measurements of electrochemical impedance spectroscopy, it is inferred that the Ag@TZPF films display almost ideal capacitive behavior with low ionic resistance within the porous structure suggesting the rapid diffusion of electrolyte ions into the porous system (Raveesha et al., 2019). Table 4 represents the comparison of the prepared material with the previous reported materials. From the table, it is clear that the proposed material shows better capacitance value and can be synthesized using low-cost method.

The prepared electrodes usually suffer in efficiency due to the accumulation of dirt over the surface. To address this issue, we developed the electrode for supercapacitors with self-cleaning nature. Contact angle measurements were carried out to analyze the wetting behavior of Ag@TZPF films. The freshly prepared Ag@TZPF film exhibited a contact angle of 64° and thereafter reduced to 21° even after 90 min UV irradiation as shown in Fig. 12. In order to check the photoinduced superhydrophilic nature of the electrodes, crystal violet (1 x 10^{-3} M) is taken as a dirt and coated over the film followed by photodegradation studies shown in Fig. 13. The crystal violet gets degraded in the presence of sunlight to smaller harmless by-products and get washed with the aid of spreading water. The hydrophilic nature indicates the easy spreading of water. This makes the surface clean without the action of an external agency and increases the efficiency of the electrode.

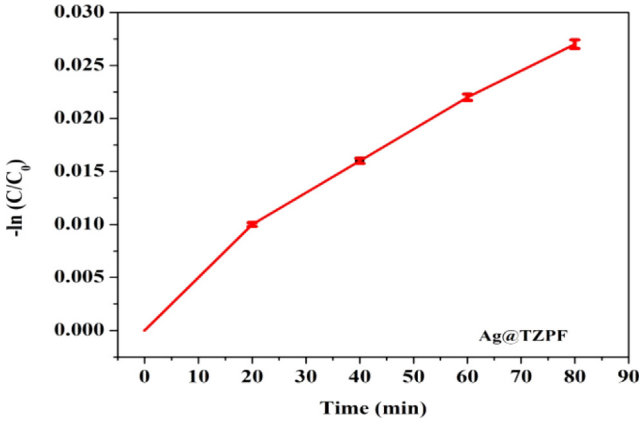

Fig. 13. Photodegradation kinetics studies of Ag@TZPF film.

The obtained results of better electrocapacitive performance lead to some perspectives on the enhancement. Herein, TiO_2-ZrO_2 nanocomposite substrates prevent Ag nanoparticles from agglomeration to increase the surface area of the entire system and also make excellent

contact between electrolytes so as to significantly reduce the diffusion and the migration of electrolyte ions. The existence of Ag nanoparticles significantly controls the overall specific capacitance by facilitating the ion hopping throughout the TiO_2-ZrO_2 composite films. Meanwhile, with the blending of ZrO_2 with TiO_2, the better chemical stability with high electrical conductivity is well preserved due to strong interaction through metal oxide bridges, which improves the accessibility of the electrolyte ions (Giri et al., 2014; Azizi et al., 2019; Park et al., 2020; Guo et al., 2019). The hierarchical porous structure with narrow pore size distribution and high surface area of the TiO_2-ZrO_2 films provide more active sites that promote fast ion transport, giving rise to huge numbers of electrical double layers being formed in terms of charge storage. This outcome implies the possibility of using the Ag@TiO_2-ZrO_2 nanocomposite film as a potential candidate to solve issues associated with electrochemical supercapacitors without affecting its efficiency and as better electrical energy storage system. Since the sol–gel synthesis method for the development of films does not entail a lengthy processing period, voluminous setup, or any particular setting, it can offer practical possibilities to overcome the scalability problem for micro/nanostructured metal/metal oxides. Furthermore, it can also be applied as a flexible technique for the easy development of hybridized metal oxides such as core–shell structures and clustered hybrids that have a high impact on electrochemical applications, catalysts and electromagnetic shielding.

4. Conclusion

Sol–gel derived ternary metal oxide Ag@TiO_2-ZrO_2 composite thin films on ITO substrates have proven for the first time to be an exceptional electrode material for the development of ideal supercapacitors. The capacitive behavior of TiO_2-ZrO_2 film is significantly enhanced with the incorporation of Ag nanoparticles. These Ag@TiO_2-ZrO_2 composite thin films can be cycled reversibly in the voltage range of 0–0.6 V, and exhibit the maximum specific capacitance of 237. 1 F/g with better capacitive retention even after 1000 cycles. This high supercapacitor behavior of Ag@TiO_2-ZrO_2 composite thin films can be attributed to the specific nature of porosity combined with a high surface area which is evident from FESEM analysis. Its high specific capacitance combined with its low-cost and eco-friendliness, provides greater benefits over other carbonaceous as well as titania based systems used to attain this goal. Also, electrochemical impedance spectroscopy was carried out to analyze the films for further supercapacitor applications. Finally, this designed concept would throw new potential ways for other energy storage devices containing different kinds of metal oxides in the field.

Data availability

No data was used for the research described in the article.

Acknowledgments

The present work was supported by DST-PURSE PII, India (SR. 417 & SR. 416 dated 27-2-2017). SMS and PVP thankfully acknowledge Mahatma Gandhi University, Kottayam, Kerala, India for providing the fellowship. Authors also acknowledge IIUCNN, Mahatma Gandhi University and SICC, University of Kerala for providing TEM and EDX analysis respectively.

References

Anil, K.M., Buzuayehu, A., Nagaswarupa, H.P., Ananda, M.H., Ravikumar, C.R., Kedir, S.F., 2020. Sci. Rep. 10, 1.
Azizi, E., Arjomandi, J., Lee, J.Y., 2019. Electrochim. Acta 298, 726–734.
Barik, R., Jena, B.K., Mohapatra, M., 2017. RSC Adv. 7 (77), 49083–49090.
Biswal, M., Banerjee, A., Deo, M., Ogale, S., 2013. Energy Environ. Sci. 6 (4), 1249–1259.
Brezesinski, T., Wang, J., Polleux, J., Dunn, B., Tolbert, S.H., 2009. J. Amer. Chem. Soc. 31 (5), 1802–1809.
Brug, G.J., Van Den Eeden, A.L.G., Sluyters-Rehbach, M., Sluyters, J.H., 1984. J. Electroanal. Chem. 6 (1–2), 275–295.
Dutta, S., Ray, C., Sarkar, S., Pradhan, M., Negishi, Y., Pal, T., 2013. ACS Appl. Mater. Inter. 5 (17), 8724–8732.
Elmouwahidi, A., Bailón-García, E., Pérez-Cadenas, A.F., Maldonado-Hódar, F.J., Castelo-Quibén, J., Carrasco-Marín, F., 2018. Electrochim. Acta 259, 803–814.
Giri, S., Ghosh, D., Das, C.K., 2014. Adv. Funct. Mater. 24 (9), 1312–1324.
Guo, Q., Li, J., Zhang, B., Nie, G., Wang, D., 2019. ACS Appl. Mater. Inter. 11 (6), 6491–6501.
Hareesh, S., Simon, S.M., Jose, T.A., Gopinath, M., Saritha, A.C., Joseph, C., Unnikrishnan, N.V., 2020. Mater. Today Proc. 33, 1396–1401.
Huang, M., Zhang, Y., Li, F., Wang, Z., Hu, N., Wen, Z., Liu, Q., 2014. Sci. Rep. 4, 4518.
Kotteeswaran, P., Raju, V.B., Murugan, A., Santosh, M.S., Nagaswarupa, H.P., Prashantha, S.C., Shivakumar, M.S., 2017. J. Energy Storage 9, 12–24.
Kumar, M.A., Nagaswarupa, H.P., Ravikumar, C.R., Prashantha, S.C., Nagabhushana, H., Bhatt, A.S., 2019. J. Phys. Chem. Solids 127, 127–139.
Li, Q., Horn, M., Wang, Y., MacLeod, J., Motta, N., Liu, J., 2019. Materials 12 (5), 703.
Li, S., Wen, J., Chen, T., Xiong, L., Wang, J., Fang, G., 2016. Nanotechnology 27 (14), 145401.
Liu, Y., Cai, X., Jiang, J., Yan, M., Shi, W., 2017. Appl. Surf. Sci. 396, 774–779.
Liu, R., Guo, W., Sun, B., Pang, J., Pei, M., Zhou, G., 2015. Electrochim. Acta 156, 274–282.
Liu, Y., Ying, Y., Mao, Y., Gu, L., Wang, Y., Peng, X., 2013. Nanoscale 5 (19), 9134–9140.
Mai, Y., Zhang, F., Feng, X., 2014. Nanoscale 6 (1), 106–121.
Mudila, H., Rana, S., Zaidi, M.G.H., 2016. J. Anal. Sci. Techn. 7 (1), 1–11.
Padmanathan, N., Selladurai, S., 2014. Ionics 20 (3), 409–420.
Pang, S.C., Anderson, M.A., Chapman, T.W., 2000. J. Electrochem. Soc. 147 (2), 444, 2000.
Park, S., Shin, D., Yeo, T., Seo, B., Hwang, H., Lee, J., Choi, W., 2020. Chem. Eng. J. 384, 123269.
Parveen, N., Ansari, M.O., Han, T.H., Cho, M.H.J., 2017. Solid State Electrochem. 1, 57–68.
Ramadoss, A., Kim, S.J., 2013. Carbon 63, 434–445.
Raveesha, H.R., Nayana, S., Vasudha, D.R., Begum, J.S., Pratibha, S., Ravikumara, C.R., Dhananjaya, N., 2019. J. Sci. Adv. Mater. Devices 4 (1), 57–65.
Reddy, M.V., Subba Rao, G.V., Chowdari, B.V.R., 2013. Chem. Rev. 113 (7), 5364–5457.
Selvakumar, D., Alsalme, A., Alswieleh, A., Jayavel, R., 2017. J. Alloys Compd. 723, 995–1000.
Simon, S.M., Chandran, A., George, G., Sajna, M.S., Valparambil, P., Kumi-Barmiah, E., Unnikrishnan, N.V., 2018. ACS Omega 3 (11), 14924–14932.
Sun, X., Xie, M., Wang, G., Sun, H., Cavanagh, A.S., Travis, J.J., Lian, J.J., 2012. Electrochemical Soc. 159 (4), A364.
Sundriyal, S., Shrivastav, V., Sharma, M., Mishra, S., Deep, A., 2019. J. Alloys Compd. 790, 377–387.
Toledo, W.D., Couto, A.B., Almeida, D.A.L., Ferreira, N.G., 2019. Mater. Res. Exp. 6 (6), 065040.
Viswanathan, V.V., Salkind, A.J., Kelley, J.J., Ockerman, J.B., 1995. J. Appl. Electrochem. 25 (8), 716–728.
Weng, Z., Guo, H., Liu, X., Wu, S., Yeung, K.W.K., Chu, P.K., 2013. RSC Adv. 3 (47), 24758–24775.
Wu, S., Liu, J., Wang, H., Yan, H., 2019a. Inter. J. Energy Res. 43 (2), 697–716.
Wu, L., Zhang, K., Zhu, X., Cao, S., Niu, D., Feng, X., 2019b. Langmuir 35 (15), 5125–5129.
Zhang, D., Chen, Y., Yu, X., Huang, H., Li, L., Wei, L., 2019. Mater. Res. Exp. 6 (8), 085044.
Zhang, Y., Li, L., Su, H., Huang, W., Dong, X., 2015. J. Mater. Chem. A 3 (1), 43–59.
Zhang, M.Y., Miao, J.Y., Yan, X.H., Zhu, Y.H., Li, Y.L., Zhang, W.J., 2022a. J. Mater. Chem. C 10 (2), 640–648.
Zhang, W., Shahnavaz, Z., Yan, X., Huang, X., Wu, S., Chen, H., 2022b. J. Inorg. Chem. 61 (38), 15287–15301.
Zhang, Z., Xiao, F., Guo, Y., Wang, S., Liu, Y., 2013. ACS Appl. Mater. Inter. 5 (6), 2227–2233.
Zhang, M., Zhou, W., Yan, X., Huang, X., Wu, S., Pan, J., Yu, X., 2023. Fuel 333, 126323.